

See discussions, stats, and author profiles for this publication at: <https://www.researchgate.net/publication/231710266>

Vibrational Study of Short-Range Order and Structure of Polyaniline Bases and Salts

ARTICLE *in* MACROMOLECULES · APRIL 1999

Impact Factor: 5.8 · DOI: 10.1021/ma981018l

CITATIONS

70

READS

12

3 AUTHORS, INCLUDING:



Philippe Colombari

Pierre and Marie Curie University - Paris 6

652 PUBLICATIONS 9,122 CITATIONS

SEE PROFILE



Sílvia Folch

Hospital Universitari de Girona Dr. Josep Tru...

18 PUBLICATIONS 213 CITATIONS

SEE PROFILE

Vibrational Study of Short-Range Order and Structure of Polyaniline Bases and Salts

Ph. Colomban,^{*,†} S. Folch,^{†,‡} and A. Gruger[†]

CNRS, UPR 1580, LADIR, 2 rue Henri Dunant, 94320 Thiais, France, and ONERA, DMSC, 92322 Chatillon, France

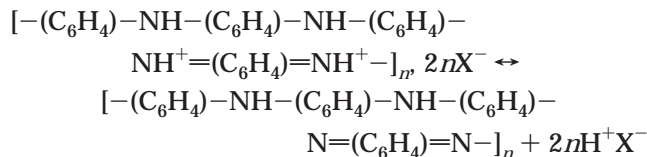
Received June 30, 1998; Revised Manuscript Received January 4, 1999

ABSTRACT: Raman and infrared reflection spectra in the backbone deformations and lattice modes range (10–1000 cm⁻¹) of EB/ES-I and EB/ES-II polyanilines are discussed and compared with those of an oligomer (BQBBa) and of the constitutive bricks of the polyaniline skeleton: diphenylamine (BB), *N,N*-diphenyl-1,4-phenylenediamine (BBB), and *N,N*-diphenyl-1,4-phenylenediimine (BQB). Short-range structure, scaling motif, and disorder are discussed. Emphasis is given to the relationship between hybridization, short-range structure, disorder, and optical properties. Ring, CH deformations, and librational/translational modes appear very sensitive to the static and dynamic disorder. Results show that vibrational spectroscopy allows to distinguish the two classes of polyaniline (ES-I and ES-II), whatever the inserted anion. The sketch of a continuous change of angle between the rigid virtual N–ring–N bond is proposed to describe the static orientational disorder.

Introduction

Over the past two decades, conducting polymers and especially polyaniline (PANI) have been the object of intensive research.^{1–4} Polyaniline is the generic term which describes the materials providing from oxidative polymerization of aniline. These materials can be used in supercapacitors,⁵ displays,^{6–8} batteries,⁹ electromagnetic shielding,¹⁰ and microwave absorbing systems¹¹ as well as for corrosion protection.^{12–15} Conductivity of PANI depends on the degree of oxidation and of protonation of the polymeric backbone. It varies over 10 orders of magnitude when the half-oxidized form, i.e., emeraldine base (EB), is fully protonated, passing from ~10⁻⁸ S cm⁻¹, in the base form, to ~10² S cm⁻¹, in the emeraldine salt (ES). This reaction, which does not change the backbone total number of electrons, is called doping, inappropriately.

Prior to discussion, it is important to note that (i) the EB compound is never as-synthesized but always obtained by acid deintercalation of the ES form and (ii) the intercalation process is reversible. In the literature, inserted protons are expected to be bound to both the amine and imine nitrogens but essentially to the latter one, due to its higher basicity,^{16,17} and a common description of the deintercalation process starting from the ideal material is



Depending upon the method of preparation, two classes of emeraldine chloride salts (ES-I, ES-II) and of their corresponding base (EB-I, EB-II) have been distinguished^{18–22} on the basis of X-ray powder patterns:

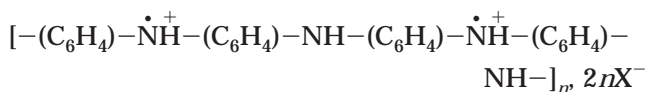
(i) ES-I is directly synthesized from oxidative polymerization of aniline in hydrochloric acid. Immersion of ES-I in aqueous base solution leads to EB-I.^{18,19}

(ii) ES-II is prepared by precipitation, in water or methanol, of solutions of EB-I or ES-I in sulfuric or methanesulfonic acids. It is then anion exchanged with 1 M HCl.²⁰ ES-II can also be prepared by protonation of EB-II. EB-II is prepared (i) by evaporation of the soluble fraction of EB-I in tetrahydrofuran (THF)¹⁹ and (ii) by uniaxially stretching of films made by evaporation of a *N*-methyl-2-pyrrolidinone (NMP) solution of EB-I at temperatures higher than *T*_g ~ 110 °C.^{21,22}

Whatever the mode of preparation, the crystallinity of EB and ES materials (class I or class II) remains low. Correlation lengths deduced from Scherrer's formula highly depend on the considered Bragg peaks and range typically from 1 to 10 nm for unstretched materials, rising up to 15 nm for cast-stretched films.^{18–22}

To date, studies of these compounds have been deeply hampered by the absence of information on their short-range structure. Particularly, no special attention has been given to the understanding of the crystallinity change associated with the (de)protonation–anion (de)intercalation process. Such “chimie douce” route gives, depending of the deintercalation process, either metastable phases with a memory of the pristine structure or amorphous phases. According to the molecular description, imine groups protonation modifies the nitrogen atoms hybridization (from sp² to sp³) and consequently the chain geometry. The modifications of the intra- and interchain short-range structures lead to the delocalization of the π system, and an electronic conductivity appears.

The backbone electronic structure in the ES form has been until now represented by a polaronic model:^{23–26}



* Corresponding author. Fax 33 1 49 78 13 23; e-mail colomban@glvt-cnrs.fr.

[†] CNRS.

[‡] ONERA.

Recently, we have undertaken an inelastic neutron

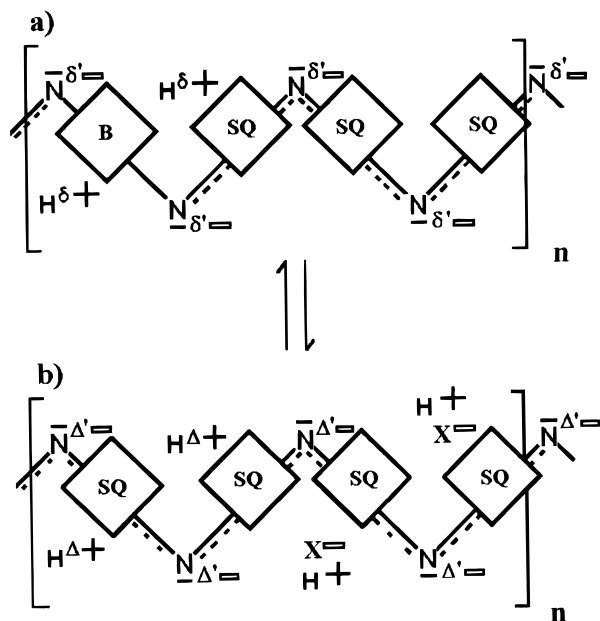


Figure 1. Scheme of the EB (a) and ES (b) forms of PANI highlighting the presence of “independent” protons. The white squares represent the volume of aromatic cycles with their π electronic cloud (SQ = semiquinoid, B = benzene ring). = represents a negative charge. δ , δ' , Δ , and Δ' symbolize the partial charges.

scattering (INS) study of EB and ES PANI forms and its deuterated-ring analogues.^{27,28} This work shows the existence at low temperature (~ 20 K), in both forms, of “independent” protons, free of covalent bond, and similar to those recently evidenced in proton conductors and intercalated graphites.^{29,30} Consequently, the usual molecular description of EB and ES polyanilines appears dramatically crude. A description in terms of nondirectionally bonded and “mechanically free” protons as sketched in Figure 1 should be more pertinent. In this description, the proton behavior looks like a “small” lithium ion. Self-doping of EB-I induced by pressure effect,³¹ lithium salt,³² and X-ray irradiation doping³³ is consistent with such a description. Competition between repulsive and attractive forces may favor more or less expanded coil and subsequently open interchain and intrachain charge carriers from internal redox reaction. These representations prevent the existence of strong, directional hydrogen bonds in EB and ES forms and, subsequently, the generation of charge carriers by means of proton transfer with water or by intrachain inversion of the $\text{NH}^+\cdots\text{N}$ bond, previously advanced^{34,35} and still discussed.³⁶ Thus, the knowledge of the chain geometry is required to explain the electrical properties. Another prerequisite is the knowledge of the modifications induced by intercalated water.^{20,27}

Our aim is the study of the short-range structure of the base and salt forms of emeraldine, combining vibrational spectroscopies (Raman scattering, infrared reflection) and X-ray diffraction analysis. Increases of the crystallinity and of the correlation length have been searched. First, we will compare the polymers and the bricks constitutive of the chemical repeat unit: diphenylamine (hereafter called BB), *N,N*-diphenyl-1,4-phenylenediamine (BBB), *N,N*-diphenyl-1,4-phenylenedimine (BQB), and the oxidized tetramer (BQBBA, a for terminal amine group). We will focus on the low- and medium-wavenumber spectra, which contain information about the short-range structure and disorder.

Attempts will be made to discriminate between geometrical and electrical, static and dynamic disorders by recording the spectra at helium temperature where the phonon population becomes small enough to limit line broadening originating from “structural” static disorder. Optical (UV-visible-near-IR) spectra, resonance profiles, microwave conductivity, and detailed X-ray results will be discussed in forthcoming papers.

Experimental Section

Samples Preparation. EB-I and ES-I Forms. Pristine emeraldine hydrochloride powders (ES-I Cl) are synthesized at 3 °C by an oxidative polymerization of $\text{C}_6\text{H}_5\text{NH}_2$, $\text{C}_6\text{D}_5\text{NH}_2$, and $\text{C}_6\text{D}_5\text{N}^{15}\text{H}_2$ aniline derivatives in 1 M aqueous HCl using ammonium peroxydisulfate as oxidant (aniline/oxidant molar ratio = 2).³⁷ The powders are converted into emeraldine base (EB-I) by treatment with a 3 wt % ammoniac aqueous solution for 2 h, followed by washing with water (~ 1000 cm³ for 5 g of powder), methanol (~ 500 cm³ for 5 g), and diethyl ether (~ 50 cm³ for 5 g). ES-I powder (5 g) is treated with 1 M HCl for 3 h to obtain a doping level of ca. 50%. Materials (EB-I, ES-I) are dried under 10^{-2} Torr dynamic vacuum until constant weight (duration ~ 4 h for 5 g).

Emeraldine dodecyl sulfate powder (ES-I DS) is prepared as described by Selvan et al.³⁸ A microemulsion is prepared with 5.3 g of water, 79.9 g of cyclohexane, 9.8 g of *n*-butanol, and 4.9 g of sodium dodecyl sulfate (SDS). Aniline hydrochloride (2.53 mmol) and ammonium peroxydisulfate (2.55 mmol) are added to separate halves of this microemulsion and mixed until they turn into clear solutions. Further mixing of the two microemulsions with vigorous agitation produces the polymerization of aniline. The polymerized microemulsion system is then left in air for 24 h without stirring. The very fine precipitated PANI salt obtained by centrifugation is carefully washed with methanol and water to eliminate any sodium dodecyl sulfate traces. Because of insufficient washing, most of the Bragg peaks assigned to emeraldine salt in ref 38 arise from contamination by hydrated SDS.

EB-II and ES-II Forms. Powder of pristine emeraldine base (EB-II) is prepared by evaporation of a solution of emeraldine base (EB-I) in tetrahydrofuran (THF), extracted fraction ~ 10 wt % of EB-I, according to the method described by Pouget et al.¹⁹ Pristine emeraldine hydrogenosulfate (ES-II HSO₄) is prepared by aqueous precipitation of a solution of EB-I emeraldine base (~ 5 g/1000 cm³) or ES-I salt (~ 5 g/1000 cm³) into anhydrous sulfuric acid (≥ 95 wt %, which correspond to ~ 5 mol of H₂O and ~ 18 mol of H₂SO₄ in 1 L of solution). After filtration on fritted funnel (pore diameter 16–40 μm), the powder is washed with water (~ 1000 cm³/5 g of polyaniline), methanol (~ 500 cm³/5 g of polyaniline), and diethyl ether (~ 50 cm³/5 g) before drying under dynamic vacuum until constant weight (duration ~ 4 h).

Anionic Exchange. Anionic exchange is made by immersion and stirring in various aqueous acid solutions (1 M) for 4 h (~ 500 cm³ for 5 g). Powder is recovered by filtration, washed with corresponding acid solution, and dried. We prepare by this way ES-I camphor sulfonate (ES-I CSA) or ES-I hydrogenosulfate (ES-I HSO₄) from pristine ES-I chloride (ES-I Cl) and ES-II Cl or ES-II CSA, from ES-II HSO₄ powder. In all cases, chemical analysis demonstrates an ionic exchange ratio higher than 90%.

Bricks of the Chemical Repeat Unit. Diphenylamine (BB) purchased from Fluka (purity 99%) is used as received, and *N,N*-diphenyl-1,4-phenylenediamine (BBB) (Aldrich, 98%) is purified by recrystallization in toluene. The *N,N*-diphenyl-1,4-phenylenedimine (BQB) is synthesized by oxidation of BBB by PbO₂.³⁹ The tetramer chloride (BQBBA Cl) is obtained by an oxidative polymerization of the hydrochloride salt of *N*-phenyl-1,4-phenylenediamine with ferric chloride hexahydrate, as described by Zhang et al.⁴⁰ Subsequent treatment of BQBBA Cl with ammonia leads to the corresponding base.

NMP-Cast Films. Films are made by dissolving the poly-aniline EB-I in *N*-methylpyrrolidinone (NMP). The solution was then cast on a glass substrate and dried in air at 110 °C. The film is unstuck with HCl (1 M) and treated with this acid for 3 h.

Pellets. Powders are pressed into pellets (diameter ~ 13 mm, thickness 0.2–1 mm) at 750 MPa for 45 min.

Techniques. The thermal stability of our materials is checked by recording the thermal expansion using an ADAMEL DI 24 (Instrument S.A.) apparatus. Heating/cooling cycles are performed in air using alumina support and rod (heating/cooling rates 120 °C/h). The pressure applied for the measure by the rod is close to 0.03 MPa which prevents from induced creep.

An XY multichannel Dilor spectrograph equipped with a liquid nitrogen cooled Wright CCD detector is used to record the Raman spectra of powders, pellets, or solutions. The Raman spectra are excited with the 632.8 nm line of an He–Ne laser. The usual 90° configuration is employed. Cycled (Air Products, USA) and lost (SMC-TBT, France) helium cryostats are also used in order to lower the sample temperature. This point will be discussed further. Long integration times, up to 1800 s, are used because of the signal weakness. Resolution is close to 15 cm⁻¹ or less. Due to the sample setting and the monochromator response, the recorded spectra have a strong VV character. VV and VH polarizations are measured using an analyzer film, the spectrum intensity being normalized versus the spectrograph response.

Reflection IR spectra are recorded using a Bruker 113V Fourier transform infrared spectrometer and converted into the dielectric function (ϵ'') using Kramers–Kronig transformation. Recordings require the pellets to be under primary vacuum at room temperature and under secondary vacuum at 20 K.

X-ray patterns are recorded with monochromatized Co K α (λ = 178.89 pm) using a Philips PW1710 automated diffractometer. The accurate positions, widths, and areas and the crystallinity fraction defined as the ratio between the sum of fitted Bragg peak area and the area of the amorphous bump are calculated by peak fitting the crystalline peaks of X-ray patterns using the 3.73 version of the Microcal Origin-fitting software (Microcal Software, Inc.). The slope and ordinate at origin are set so that the linear baseline coincides with the spectrum wings. Another prerequisite to launching the fit is to initialize the program with the number of peaks that should be taken into account as well as their estimated form (Gaussian or Lorentzian) and width.

Peak fitting of Raman spectra and of the dielectric function is made in the same manner in order to calculate peak position and width.

Visualization of polymeric chain geometry is made using the Unichem software of Cray Research.

Results and Discussion

Before discussing the Raman and IR spectra, we will consider the problems arising in the analysis of colored, more or less conducting materials with limited thermal stability.

1. What Are We Observing? *1.1. How To Record the Raman Spectrum of Colored, Low Thermal Stability Materials.* According to earlier works on the thermal stability of PANI bases and salts,^{41–43} thermal expansion curves (Figure 2) show that the emeraldine base is a thermally stable polymer up to ca. 300 °C (Figure 2a). The glass transition is however observed at ca. 150 °C with a characteristic thermal expansion bump. The protonated forms are significantly less stable, and their stability limit depends on the counterion: the deprotonation of the chloride salt in air starts at ca. 50 °C, as evidenced by the dilatometric curve given in Figure 2b and by previous conductivity measurements,³¹ whereas that of the camphor sulfonic acid salt (CSA) occurs above

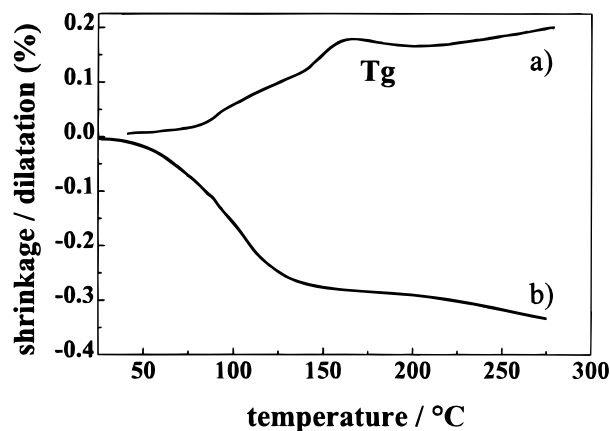


Figure 2. Thermal expansion: (a) EB-I emeraldine pellet and (b) ES-II emeraldine chloride pellets (T_g = glass transition peak).

200 °C.⁴⁴ Consequently, deprotonation of chloride salt takes place at the pellet surface at room temperature, and a hydrogen/anion gradient may occur in the near-surface region as usually observed in proton conductors.⁴⁵ This phenomenon would be enhanced in a vacuum by the volatility of the intercalated acid.

Raman spectrum recordings easily provoke local heating of colored materials and hence could enhance the deprotonation of salts, especially if the volatility of the corresponding acid is high. To limit the materials evolution, we kept the laser power below 2×10^5 W/m². Besides, well-densified pellets were used in place of powder to improve the thermal dissipation ability. The huge temperature rise induced by laser irradiation in the (pre)resonance condition is evidenced by measurements in helium cryostats. Figure 3 gives a typical example. At first sight, the Raman spectrum of a ES-I Cl pellet in a lost helium cryostat, recorded under 1.4×10^5 W/m² (Figure 3b), does not correspond to the one expected for a sample at 10 K, the temperature measured by the probe located in the sample compartment. Using the Stokes (S) and anti-Stokes (aS) bands, the sample temperature can be estimated, because of the weak resonance effect with the 632.8 nm exciting wave, from the intensity ratio of the corresponding bands according to the simplified Boltzman equation:

$$\frac{I_S}{I_{aS}} = \exp\left(\frac{h\nu c}{kT}\right)$$

where h is the Planck constant (6.63×10^{-34} J s), k the Boltzmann constant (1.38×10^{-23} J K⁻¹), c the light speed (3×10^{10} cm s⁻¹), and ν the considered wavenumber. For $\nu = 200$ cm⁻¹, the theoretical intensity ratios calculated at 293, 100, and 50 K are respectively 0.375, 0.055, and 0.003. The experimental value being higher than 0.05, the sample temperature is higher than 100 K. A temperature close to 50 K (the anti-Stokes band at 200 cm⁻¹ has disappeared (Figure 3c)) is only achieved when the whole pellet is plunged into liquid helium, the laser beam reaching the sample through the liquid helium. This shows that a high level of cooling is needed to compensate the local heating induced by the laser illumination, whatever the illumination power used. On the contrary, inelastic neutron scattering can be effectively recorded at 20 K using sealed sample holders, without any local heating due to neutron beam illumination.

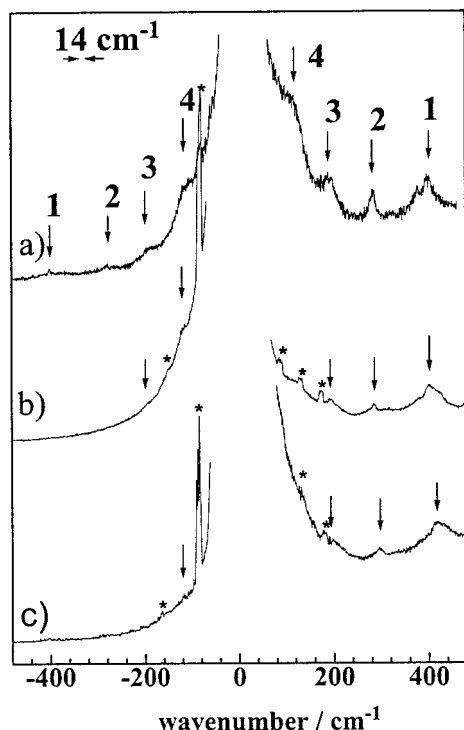


Figure 3. Raman spectra ($\lambda_{\text{exc}} = 632.81$ nm) of ES-I emeraldine chloride pellet recorded in different conditions: (a) room temperature, laser power 0.7 mW; (b) "helium temperature", temperature measured by the probe located in the sample temperature: 10 K, laser power 7 mW; (c) sample immersed in liquid helium, laser power 7 mW. Asterisks indicate plasma bands. Arrows indicate the Stokes and anti-Stokes bands.

1.2. Short-Range Order, Scaling Motif, and Crystallinity. Various kinds of heterogeneity are expected in EB and ES forms. X-ray diffraction clearly evidences that different degrees of organization are present.^{18–22} In the "crystalline part", a strong interchain Coulombian coupling is expected through the ordered anions while in the "amorphous part", despite the large chain disorder, a significant interchain coupling should remain as evidenced by the high mechanical strength of a film.⁴⁶ The model of metallic islands where charge hopping dominates, embedded in a poor conducting zone, has been used, but identification between metallic islands^{49–51} and crystalline regions^{19,22,52} has failed to date. In fact, the correlation length and "crystallinity" highly depend on the synthesis of the pristine materials and its following history. Note that many authors speak of "crystalline parts" recognized by more or less extended correlation lengths deduced from X-ray Bragg peak broadness using Scherrer's formula. This does not imply that "ordered" and "amorphous" regions make a pavement of the real space. Assuming the crude model that the peak broadening arises from limited crystallite size and not from the paracrystal description (see below), the largest correlation lengths are calculated from the bandwidth at half-height of ES-II salts, using Scherrer's formula. We find about 15 nm for the 0.47 nm peak of pristine ES-II sulfate and close to 10 nm for the 0.88 nm peak of the ES-II chloride, obtained by ionic exchange of ES-II sulfate in HCl (pH = 1).

Von Hoseman and Guinier^{47,48} considered correlation length in low crystalline materials a long time ago. They proposed the sketch of the "paracrystal" as a continuous deformation of the periodic crystal structure by replacing the constant cell edges by statistically determined

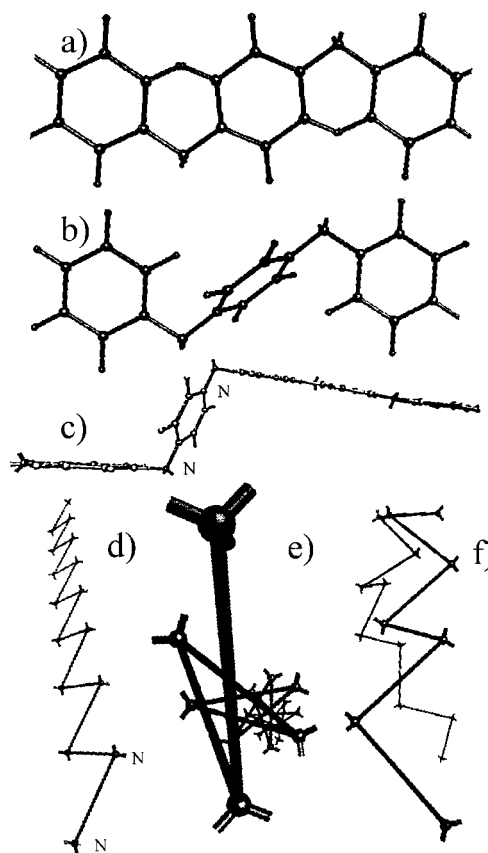


Figure 4. Polyaniline chain with a reduced (a, $\varphi \sim 0^\circ$) or a large (b, $\varphi \sim 75^\circ$) dihedral angle; (c) trans-left-trans disorder ($\phi_1, \phi_2 = \pm 60^\circ$); artist views of the rigid virtual bond (N-ring-N) alternations leading to (d) a regular chain (from $n = 1$ to n , $\phi_n = 0^\circ$), the possible directions of the chemical bond are sketched by small ribbons, (e) a helical chain (from $n = 1$ to n , $\phi_n = 30^\circ$), and (f) a buckle chain (from $n = 1$ to n , $\phi_n = \pm 30^\circ$) with φ and ϕ_n respectively the dihedral angle (angle of the phenyl moieties relative to the plane of the nitrogen backbone) and the torsion angle of the n th virtual bond relative to the $(n - 1)$ th, $(n - 2)$ th plane.

vectors varying in length and direction. The individual cells thereby become deformed, and so does their content. The same scaling motif can be repeated over a limited distance, whatever the origin used. Thus, the sketch of a continuously connected array with a continuous change of angle and bond length within a certain limit appears more realistic than the irregular pavement of amorphous and crystalline region.

2. Hybridization and Short-Range Structure: An Origin of the Geometrical Disorder. From a molecular point of view and owing to the sp^2 and/or sp^3 type of the nitrogen atoms which are located between the rings of the backbone, polyaniline may have a wide variety of forms, conformationally and structurally (Figures 4–6). For any given polyaniline oxidation state, an interesting aspect of this phenomenon is the large degree of conformational variation originating from the torsional orientation of the benzenoid rings. On one hand, considering two subsequent ones, steric hindrance between the two close-lying aromatic hydrogen atoms favors a large dihedral angle (φ), angle of the phenyl moieties relative to the plane of the nitrogen backbone, up to 90° (Figure 4b). On the other hand, energetical stabilization, i.e., large π -electronic overlap through the nonbonded orbitals of the intermediate nitrogen atom, is favored when the angle is reduced (Figure 4a).

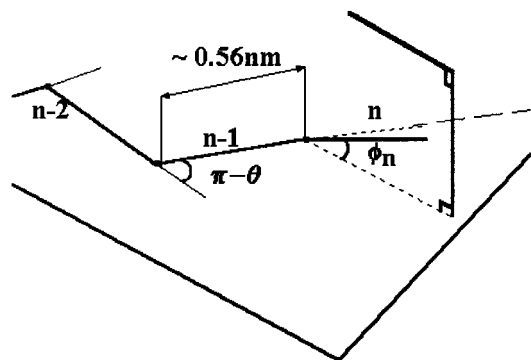


Figure 5. Virtual bonds between nitrogen atoms; n th bond notated at angle ϕ_n with respect to plane formed by $(n-1)$ th and $(n-2)$ th bonds.

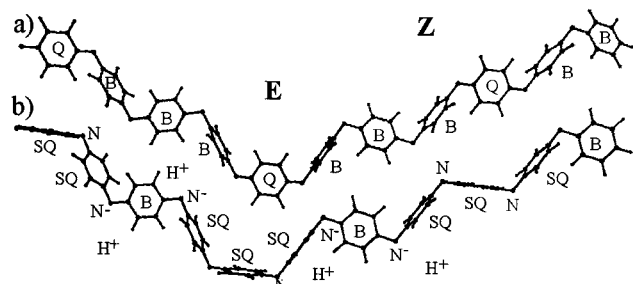


Figure 6. Z and E configurations of ideal emeraldine base in its (a) ground state and (b) excited state (E called previously *cis* and Z *trans*).

In addition to the dihedral angles between two benzenoid nearest neighbors, a geometrical description of a polyaniline chain has to take into account the angle θ between neighboring N–ring–N segments of length approximately equal to 0.56 nm (which corresponds to ~ 0.47 nm for its projection along the chain axis (Figure 5)). Depending on the hybridization of the nitrogen sites, i.e., the π -bond character of the $C_{\text{ring}}\text{--N}$ bond, θ ranges from 110° to 120° , as expected for pure sp^3 or sp^2 hybridization. Furthermore, each N–ring–N bond, which can be considered as a rigid virtual bond, is allowed to sweep out a cone of possible orientation, leading to a lot of conformations locally and/or gradually disordered. Deviations to an all-trans backbone conformation (Figure 4d) can be defined by the torsion angle of the n th virtual bond relative to the $(n-1)$ th, $(n-2)$ th plane, i.e., $(\phi_n)^+$ or $(\phi_n)^-$ according to whether the rotation is made on the left (–) or on the right side (+). An all-trans zigzag segment form, from $n=1$ to the n th bond, is characterized by $\phi_n = 0^\circ$. Rough local disorder implies long segments (all-trans zigzag backbone sequence) cut by left-handed defects as *trans-left* (at least three consecutive virtual bonds-chain, deviation $\phi \pm 120^\circ$) and *trans-left-trans* (at least five consecutive virtual bonds blend of the chain, the trans segments on both side of the defect remaining almost parallel). Figure 4c illustrates this type of disorder. Continuous disorder supposes progressive deviations along the all-trans zigzag segment. Consecutive equal deviations in the same direction lead to a linear chain segment with a helical structure (Figure 4e). On the contrary, equal alternative deviations provide neither linear nor compact chain segment. We can expect that deviations of $\phi = 30^\circ$ in any direction are energetically favorable. They permit large π conjugation through the unbonded nitrogen orbitals. Progressive disorder obtained from $\pm 30^\circ$ deviations in a chain segment of nine virtual bonds

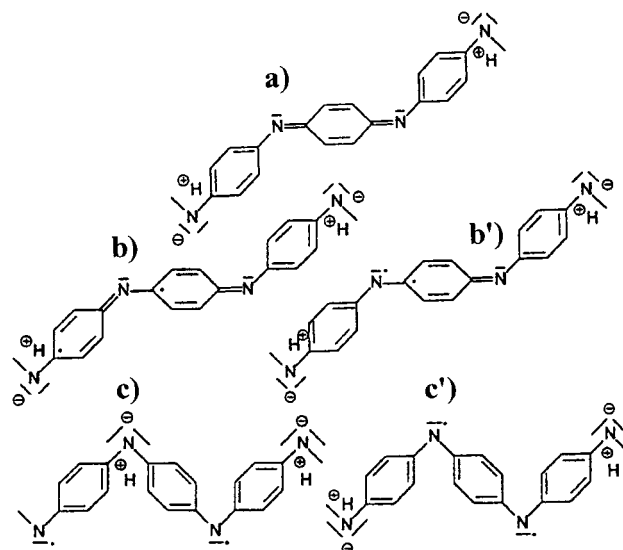


Figure 7. Molecular models: ground state of EB (a); excited state: the electron is coming from the neighboring benzenoid moieties (b) and from the lone pair of an imine nitrogen (b'); “ES-like” EB (c) and after internal redox conversion (c).

has been represented in Figure 4f. So, depending on the nature and the number of the rough defects and of the left-handed importance of the progressive disorder, more or less linear (Figure 4d), helical (Figure 4e), or expanded coil (Figure 4f) structures will be expected.

While ES backbone is expected to be constituted (at least in his conducting part, using the molecular model) by semiquinoid rings with ca. sp^3 nitrogen atoms, the EB polymer chain configuration seems at first sight radically different. Indeed, due to the sp^2 hybridization of the imine nitrogen atoms incorporated in the BQB units, the ring–N–ring planes on both sides of the quinoid ring and the quinoid itself (which is almost planar) are coplanar. Owing to steric hindrance and π system overlap, a dihedral angle (φ) close to 90° relative to this plane is expected for the benzenoid rings. Z and E configurations (previously called *trans* and *cis* configurations) of EB polymer in its ground state have been represented in Figure 6a. In fact, optical spectra of EB as well as of corresponding oligomers do not agree with this structure. Two bands are observed at ca. 4 eV and at ca. 2.2 eV. The former is characteristic of aromatic compounds and originates undoubtedly from $\pi\text{--}\pi^*$ transitions delocalized in individual phenyl moieties.^{53,54} The latter is a broad absorption in the visible region. Its low energy suggests that it encompasses electron and hole orbitals extending over more than one phenyl moiety. In the excited state, the electron provided by (i) the neighboring two benzenoid moieties⁵³ or (ii) the lone pair of an imine nitrogen⁵⁵ is trapped in the quinoid ring (Figure 7). Whatever the origin of the electron, its promotion needs serious distortion of the BQB ground-state structure. It corresponds to a molecular exciton characteristic of the BQB sequence. CNDO/S3 and MNDO molecular orbital calculations^{53,56} lead to the conclusion that energy absorption lower than 4 eV occurs only when the quinoid ring is twisted out of the CNC plane. Thus, the excited state of the BQB group is geometrically different from its ground state, and the 2.2 eV absorption has to be associated with a locally distorted BQB molecular conformation (Figure 6b). Exciton formation requires twists of the three rings around the rigid N–ring–N virtual bond and forces the

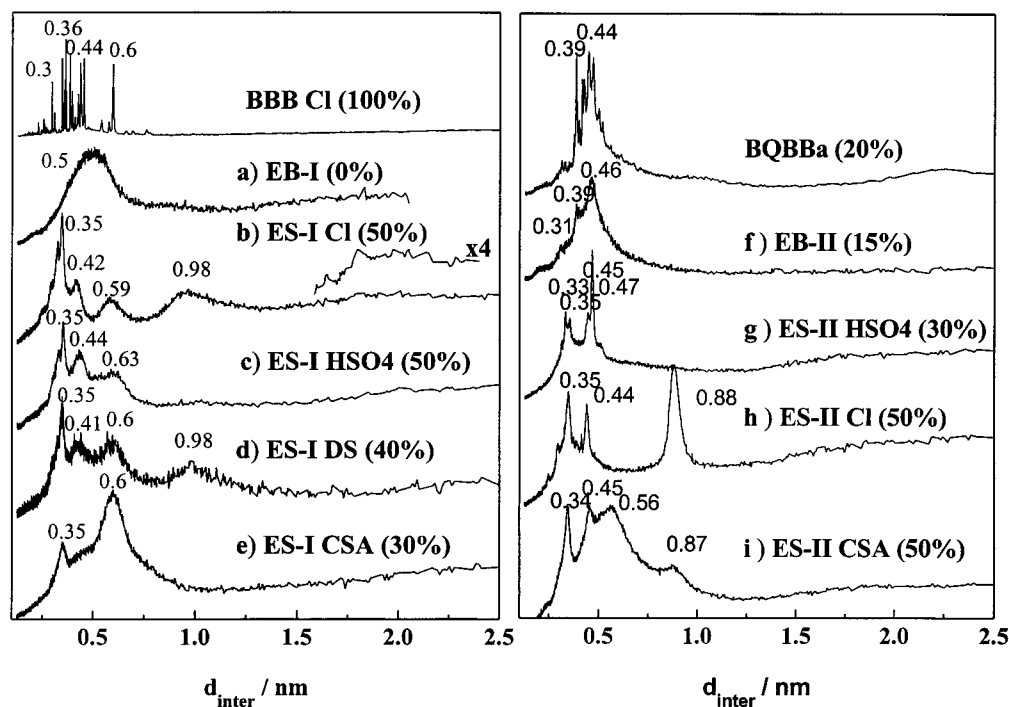


Figure 8. X-ray powder patterns of (a) emeraldine base film; (b) ES-I emeraldine chloride (direct synthesis); (c) ES-I emeraldine sulfate prepared by ionic exchange of powder shown in (b); (d) as synthesized ES-I emeraldine dodecyl sulfonate (microemulsion); (e) ES-I emeraldine camphor sulfonate prepared by ionic exchange of powder shown in (b); (f) emeraldine base pellet of THF-soluble EB-I (EB-II type); (g) ES-II emeraldine hydrogenosulfate (precipitated from EB-I solution in anhydrous sulfuric acid); (h) emeraldine chloride prepared by ionic exchange of ES-II hydrogenosulfate; (i) emeraldine camphor sulfonate prepared by ionic exchange of ES-II hydrogenosulfate. Powder patterns of BBB chloride and BQBBa are given. For comparison, crystallinity ratios are given in brackets.

BQB rings to adopt a semiquinoid geometry, with a central partially double C–N bond. Limit configurations assume that electronic delocalization concerns the BQB sequence only. Minimum energy is obtained by rotating the quinoid ring by $\varphi = 90^\circ$. In that conformation, π overlap between π_B and π_Q orbitals through the sp^2 nonbonded nitrogen orbital becomes possible.

These excited EB configurations are expected to be very long-lived because of the large inertial mass involved for relaxation (with rotation of semiquinoid ring) to the ground state and of the “high” compactness of the materials. Consequently two separated units are expected in the EB material and corresponding oligomers: a sequence constituted by three conjugated rings of the semiquinoid type and (in the idealized form) a *p*-diaminobenzene ring which acts as a bolt, preventing extension of the trapped electron to the whole backbone. It is not surprising then that pressure³¹ or radiation³³ provokes in EB compounds a decrease of the excitonic transition energy and, subsequently, a conductivity increase, by several orders of magnitude in relation to the geometrical change of the polymeric chain. Such evolution is illustrated with a limit formula in Figure 7.

In Figure 6b, we recognize the polyelectrolytic behavior of the backbone. The difference between “ES-like” EB and ES compounds is a consequence of the ionic field surrounding the polymer backbone. In the ES compound, it partly consists of a negative ion, while in EB it only consists of protons. The presence of negative entities acts as repulsive forces and favors extension of the inter- and intramolecular order, i.e., of the delocalization of the polaronic species. On the contrary, protons act as attractive forces and favor the disordered backbone chain. This discussion clearly demonstrates that

the geometry of the polymeric chain is intrinsically a function of the electronic delocalization and of the acid intercalation. This may induce specific features in the spectral regions involving deformation and lattices modes

3. Evidence of Various Structures. Although it was recognized by Pouget¹⁹ a few years ago, the origin of the polymorphism (class I and class II) is not understood. The fact that the form seems to depend on the synthesis route, and not the anion, makes us think that it is due to the arrangement and the nature of chains (length distribution, regularity of the phenyl/(semi)quinone alternation, regularity of the θ , ϕ alternation), which is fixed in the pristine materials and, to some extent, modified by the following steps such as uniaxial film stretching, deintercalation, and the size and the shape of anions, in other words, the history of the materials. Thus, we will try to compare spectra of typical samples.

3.1. X-ray Evidence of Various Forms. Before any discussion of the vibrational spectra, it is important to identify the allotropic forms, from X-ray powder patterns, so that comparison could be made with literature. In Figure 8 are reported X-ray powder patterns typical of the class I and class II EB and ES materials: pristine ES-I Cl powder and its deprotonated EB-I form (Figure 8a,b), microemulsion prepared ES-I DS powder (Figure 8d), EB-II powder obtained from EB-I powder solution in THF (Figure 8f), pristine precipitated ES-II HSO₄ powder (Figure 8g), anionic exchanged ES-I or ES-II derivatives: ES-I HSO₄ and ES-I CSA (Figure 8c,e), ES-II Cl, ES-II CSA (Figure 8h,i). To highlight the common interreticular distances and to compare the correlation lengths, X-ray patterns are directly plotted as a function of the interreticular distance. Note that the Lorentz

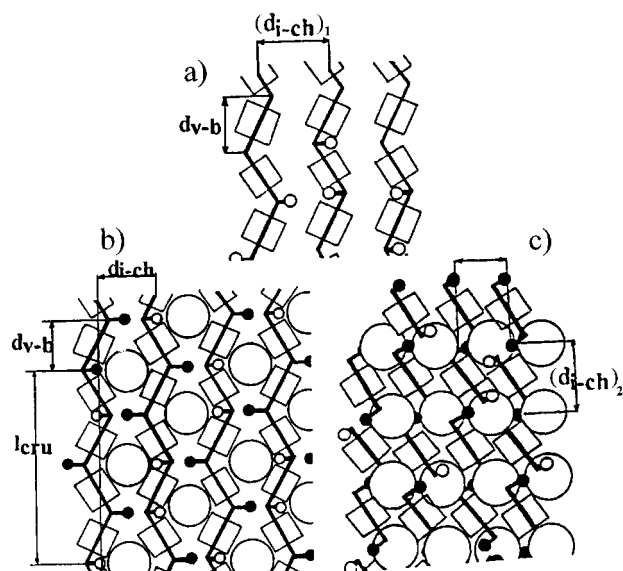


Figure 9. Scheme of in-phase (a) and out-of-phase (b, c) zigzag chains. The volume of the aromatic cycles is shown (squares). Small black and white circles correspond to proton sites associated with nitrogen atoms according to the macromolecular model. Large circles correspond to an anion. d_{v-b} is the projection of the virtual bond distance along the chain axis, d_{i-ch} the projections of the interchain distance, and l_{cru} the projection of the chemical repeat unit length.

polarization correction has not been made and that the part above 1 nm is consequently enhanced. The used setup is more pertinent than the usual 2θ angular plot to give a clear perception of the correlation length decrease with increase of the interreticular distance. The difference in broadness observed for the different reflections shows that the disorder is very anisotropic. The very low intensity of the peak above 1 nm indicates that the effective chemical unit is limited to a two-cycle sequence, according to the models built with a rigid virtual N–ring–N segment and given for example in Figures 4 and 5. The semiquinoid/benzenoid alternation in EB is therefore averaged by the electrical or geometrical disorder. On the contrary, the geometric arrangement at a scale shorter than the virtual bond projection $d_{v-b} \sim 0.47$ nm (Figure 9) and the interchain distance appears to be well-defined. Thus, it can be expected that the spectroscopic cell will be limited to a two-cycle repeat unit and its first neighboring shell. The Bragg distances and corresponding unit-cell parameters calculated according to the Pouget description will be discussed in a forthcoming paper. Crystallinity ratios are however given in Figure 8. A comparison with the X-ray powder pattern of BBB chloride and with BQBBa tetramer gives evidence of the common interreticular distances within the virtual bond range, related to the same building bricks.

EB-I and EB-II Materials. The pristine EB-II form (Figure 8f) exhibits significant crystallinity ($X_c = 15\%$), whereas the EB-I form (Figure 8a), obtained by ES-I deprotonation in ammonia solution, is totally amorphous. This result agrees with that of Pouget et al.,¹⁹ who indexed all the EB-II Bragg reflections with an orthorhombic lattice (*Pbcn* structure, space group D_{2h}^{14}). The Bragg peaks of our diffractogram indicate a slightly larger unit cell than the one they found. In the description, the zigzag repeated unit contains only two aromatic rings ($c = 1.04$ nm). Figure 9 shows a sketch of the possible chain packing along the orthogonal projection

of out-of-phase and in-phase models. Squares represent the volume of the aromatic rings with their π electron cloud.

ES-I and ES-II Materials. The hydrochloride salts (ES-I and ES-II) diffractograms (Figure 8b,h) are very similar to those of Pouget et al.,¹⁹ except for the small bump observed in the 1.7–2.2 nm range, which will be discussed below. They have proposed an ES-II orthorhombic structure, *Pc2a* (C_{2v}^8), composed of layers of polymer chains alternating along the b axis with layers of the Cl anions. Polymer chains are expected to be perpendicular to the (a,b) plane. Two successive chains along a have their zigzag backbone out-of-phase (Figure 9a). A monoclinic symmetry (space group $P2_1$) has been proposed for the ES-I form: the unit cell contains a single zigzag unit and one anion; chains are in-phase (Figure 9b). Using usual C–C and N–C distances, the projection along the chain axis of the virtual bond d_{v-b} is equal to 0.42–0.48 nm as a function of the θ angle. The interchain distance d_{i-ch} , according to a dense geometrical packing between Cl and aromatic cycles, is close to 0.59 nm. The closest interreticular distance between layers formed of adjacent chains is 0.35 nm.

In a preliminary report,²⁰ we have shown that weak peaks are observed in the 1.7–2.2 nm range, which have not been observed by Pouget et al.¹⁹ Similar reflections ($d \sim 2$ nm) have been observed for the poly(*o*-toluidine)⁵⁷ and for CSA films cast from *m*-cresol.^{58–61} This additional reflection may correspond to the doubling of the unit cell previously proposed¹⁹ or to an alternate ordering of PANI and anions layers.^{58–61} However, the interplanar distance being very similar for salts of various size anions, the assignment of this low angle peak to c axis periodicity appears more consistent in lack of accurate structure determination.

3.2. Anion Exchange and Pristine Structure. A memory effect remains when ion exchange is made: samples keep their structural form, e.g., from ES-I Cl to ES-I HSO₄ and from ES-II HSO₄ to ES-II Cl (Figure 8). This may indicate that the “crystalline class” is fixed on synthesis. However, the X-ray patterns of polyanilines CSA, obtained by anion exchange from hydrochloride ES-I and ES-II, show slight differences with those of the ES-I and ES-II class. Thus, the insertion of the bulky anion in the material might induce a little change of the chain geometry: for instance, the X-ray pattern of the ES-II CSA, obtained by ion exchange of ES-II HSO₄, looks like that of PANI CSA prepared using *m*-cresol as solvent.^{58–61} In fact, anion-exchanged ES-II CSA seems to be a mixture of the ES-I CSA and of the ES-II CSA, Cl like forms.

The as-synthesized powder ES DS, with a long chain anion (dodecyl sulfate), belongs to the ES-I form, and its crystallinity does not increase significantly for materials prepared using the microemulsion route, for which the length of polymeric chains is expected to be short. The increase of crystallinity is however straightforward for materials with very short chains (EBII, BQBBa).

3.3. Prediction of the Vibrational Spectra. Amorphous EB-I and “Crystalline” EB-II Forms. The IR and Raman spectra of the quasi-amorphous or totally amorphous EB-I and EB-II regions are not subject to any selection rules, whereas the “regular” chain configuration in the crystalline EB-II region may give rise to some selection rules. We will first consider the spectrum expected from the crystalline region of EB-II emeraldine base.

Table 1. IR and Raman Mode Numbers Expected and Observed for EB-I/EB-II, ES-I, and ES-II Pellets^a

	EB-I/EB-II		ES-I			ES-II		
	no. expected	no. obsd	no. expected	no. expected	no. obsd	no. expected	no. expected	no. obsd
repeat unit	C ₁₂ H ₈ N ₂		C ₁₂ H ₈ N ₂	C ₂₄ H ₁₆ N ₄		C ₁₂ H ₈ N ₂	C ₂₄ H ₈ N ₂	
internal modes	120	~43	60	126	~35	120	252	~33
external modes	9	4 1 ^b	6	9	4 1 ^b	15	33	2 1 ^b

^a $\lambda = 632$ nm for ES-I and ES-II, $\lambda = 458$ nm for EB-I/EB-II. ^b Overdamped mode leading to the Rayleigh wing.

Table 2. IR Reflectivity, Raman, and INS Band Wavenumbers and Assignments in the Deformation and Lattice Mode Range for Base Forms^e

IR ^a			Raman ^b				THF soln	INS ^c EB-I	assignments
EB-I		EB-II	EB-I		EB-II				
H	D	ρ^d	H	H	D	ρ^d	H	H	
851 sh	752 m	1.13	848 sh						γ_{CH} (11)
				841 w			839 w	838 w	ring def (d)
830 s	740 m	1.12	831 s						γ_{CH} (11)
807 sh	715 sh	1.13	801 sh	815 sh					γ_{CH} (11)
775 w				781 m	742 m	1.04	783 m	780 m	ring def (d)
745 vw				748 m	683 m	1.10	747 m	748 m	ring def (d)
539 sh	470 w	1.15	543 sh	539 sh	473 m	1.14			
528 sh	456 sh	1.16	529 sh	525 m	459 m	1.14	524 m	525 m	γ_{CC} (16b)
509 m	437 m	1.16	506 m	506 sh					
				439 w			441 w	442 w	
415 m	368 m	1.13	415 m	418 m	368 m	1.14	417 m	417 m	γ_{CC} (16a)
364 w			360 w	368 vw	335 vw	1.09	366 vw		
				270 vw	249 vw	1.08		265 vw	
152 w	148 w	1.03	155 w						
				136 w	136 w	1		139 w	
100 w	100 w	1	100 vw						
80 w	80 w	1	75 w					142 w	
								102 b	

^a Reflection IR spectra converted into dielectric function by Kramers–Kronig transformation, room temperature. ^b 633 nm exciting wavelength, room temperature. ^c 20 K inelastic neutron scattering from refs 27 and 28. ^d Isotopic ratio. Alone the rings are deuterated. ^e s = strong, m = medium, w = weak, vw = very weak, sh = shoulder, b = broad.

For a point group D_{2h} (D_{2h}^{14} space group), we expect $3 \times 22 \times 2 = 132$ normal modes, considering two chains by a spectroscopic unit cell and a repeat unit which consists of C₁₂H₈N₂: three translations of the whole unit cell, i.e., acoustical modes, nine lattice modes, and 120 [$2 \times (3 \times 22 - 6)$] internal vibrations are expected (Table 1). The vibrations, which are active in infrared, are inactive in Raman spectra and vice versa because of the center of symmetry. It is the mutual exclusion rule. Some general rules concerning the IR and Raman activity of librations and translational vibrations of molecules, in a crystal lattice, might be valuable. In particular, molecules with a C_i site symmetry or point group containing the inversion operator do not possess translational vibrations in Raman-active species, and they do not have librations in IR-active species.

"Crystalline" ES-I and ES-II Forms. If we consider the cell doubling, the repeat unit of ES-I and ES-II salts consists of C₂₄H₁₆N₄. The crystalline region of the ES-I form, according to Pouget,¹⁹ is monoclinic, space group $P2_1$, with one chain and two anions by unit cell. We do not expect any IR/Raman exclusion. There are $3 \times (44 + 2) \times 1 = 138$ degrees of freedom: 126 [$1 \times (3 \times 44 - 6)$] internal modes, three acoustic modes, and nine external modes (Table 1). As for the ES-II form, it has been described with orthorhombic symmetry.¹⁹ Its space group is $Pc2a$ (C_{2v}^8), with two chains and four anions by a primitive cell. No exclusion is envisaged. We expect $3 \times (44 + 2) \times 2 = 276$ normal modes. These modes could be divided in three subgroups: 252 [$2 \times (3 \times 44 - 6)$] internal modes, three acoustic modes, and 33 lattice modes (Table 1).

The above discussion has demonstrated that the common motif consists of two consecutive virtual rigid

bonds. So, we expect $3 \times (22 + 1) \times 1 = 69$ normal modes for the ES-I form, divided into 60 [$= 1 \times (3 \times 22 - 6)$] internal modes, three acoustic modes, and six external modes and $3 \times (22 + 1) \times 2 = 138$ normal modes for the ES-II form, divided in 120 [$2 \times (3 \times 22 - 6)$] internal modes, three acoustic modes, and 15 external modes (Table 1).

Although the number of external bands appearing on a powder spectrum is usually lower than the calculated number (Table 1), the number of bands in the lattice mode range would be for the ES-II form than for EB or ES-I forms. The differentiation between ES-I and EB-I/EB-II forms seems to be difficult on the basis of the number of modes. However, the change from a nearly nonpolar structure (EB form) to an ionic salt (ES form) will be very important for the band intensities, especially for the IR spectrum.

3.4. Spectroscopic Evidence of Various Forms. (1) The low wavenumber IR and Raman bands contain information both on the intramolecular configuration and on the arrangement of molecular bricks within the materials. (2) The high wavenumber range is indicative of the nature of chemical bond and has already been intensively discussed.^{62–65}

From the vibrational point of view, the disorder can result from an irregular arrangement of chemical bonds as well as from the presence of electrical defects. In a crude approximation, we can consider that stretching modes are very sensitive to electrical disorder, whereas orientational disorder of polymeric backbone would affect essentially bending and external modes. Thus, we will focus our attention on deformation and external modes which contain information on the short-range structure (Figures 10–12 and Tables 2, 3).

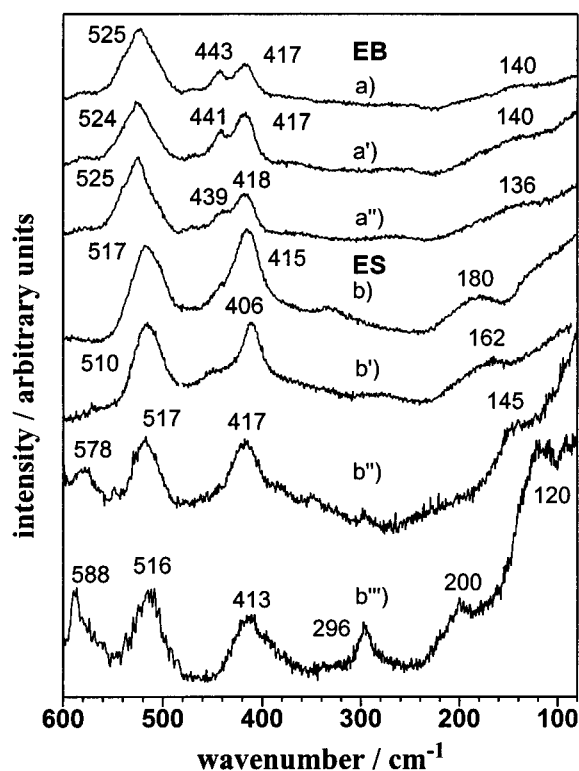


Figure 10. Room-temperature Raman spectra (632.81 nm illumination, $P = 1$ mW) in the 600–100 cm^{-1} region of (a) EB-I solution in THF; (a') EB-II emeraldine base pellet; (a'') EB-I emeraldine base pellet; (b) EB solution in anhydrous $\text{CH}_3\text{SO}_3\text{H}$; (b') EB solution in anhydrous H_2SO_4 ; (b'') ES-II emeraldine chloride pellet prepared by ionic exchange of hydrogensulfate analogue; (b''') ES-I emeraldine chloride pellet.

The ES-I and ES-II compounds can very easily be distinguished from their Raman spectra, whatever the inserted anion, e.g., Cl , HSO_4 : a spectrum of an ES-I salt presents two bands at 200 and 120 cm^{-1} (Figure 10b''') and the one of an ES-II form a characteristic band at ca. 145 cm^{-1} (Figure 10b'). These Raman modes are assigned to the deformations of the $\text{C}_{\text{ring}}\text{--N--C}_{\text{ring}}$ groups with more or less coupled ring motions. Indeed, the spectrum of BB (Figure 12), a two-ring reduced compound, exhibits four bands between 309 and 130 cm^{-1} that have been assigned to these vibrations.^{66,67}

The low IR and Raman wavenumber spectra of ES-I form show IR/Raman mutual exclusion (Figures 10b''' and 11d) which indicates that the ES-I structure has a center of symmetry. An IR/Raman exclusion is also observed between the spectra of EB-I (X-ray amorphous) and EB-II materials (poorly crystalline materials) (Figures 10a', a'' and 11a, a'). This indicates a center of symmetry for the corresponding spectroscopic unit. Thus, the origin of the structure difference can be related to the pristine zigzag chain arrangement and not to the site occupancy of the anion. On the other hand, the observation on IR and Raman spectra of ES-II of bands at about the same wavenumbers (Figures 10b''–11d'') evidences a noncentrosymmetric structure. These results are in agreement with the space groups proposed by Pouget¹⁹ for EB-II and ES-II forms, respectively $Pbcn$ (D_{2h}^{14}) and $Pc2a$ (C_{2v}^8), but not for the ES-I form. The presence of a center of symmetry in the EB-I and ES-I forms leads to a structure with out-of-phase zigzags (Figure 9b). On the other hand, due to the observation of IR and Raman modes at the same

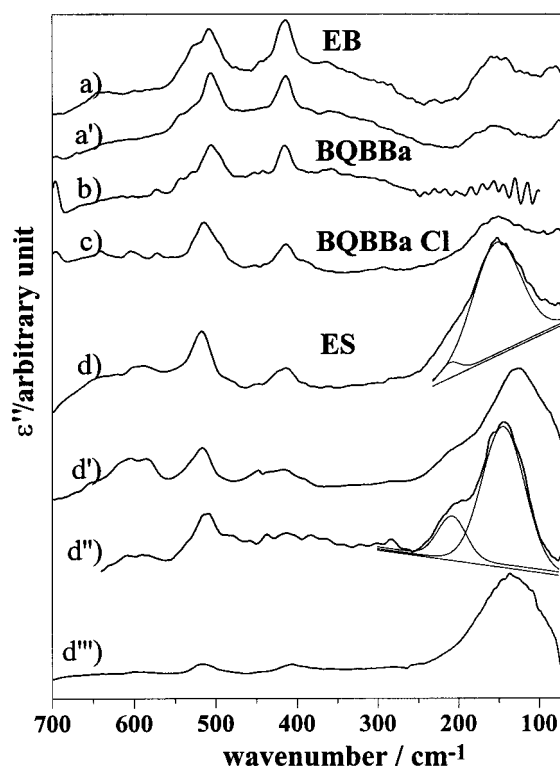


Figure 11. Low-frequency ϵ'' function obtained by the Kramers–Krönig conversion of room-temperature reflection spectra of (a) EB-I emeraldine pellet, (a') EB-II emeraldine pellet, (b) tetramer base, (c) tetramer salt, (d) ES-I emeraldine chloride pellet, (d') ES-I emeraldine dodecyl sulfonate pellet, (d'') helium liquid temperature spectrum of emeraldine ES-I chloride pellet, (d''') ES-II emeraldine chloride pellet (room temperature). Examples of spectral decomposition are given.

frequency for the ES-II form, the in-phase arrangement appears more likely.

The mode numbers expected (see section 3.3) and observed are different for all forms (Table 1). This result shows that a two-cycle chemical unit is sufficient to describe these materials. The internal mode number is approximately the same for the ES-I and the ES-II forms. For the external modes, because of the IR/Raman exclusion, there are two times as many bands for ES-I as for ES-II.

3.5. Ring Deformations and Chain Orientational Disorder. In Tables 2 and 3, the γ_{CC} , δ_{CC} , and γ_{CH} vibrational modes of EB and ES materials observed in the range 850–400 cm^{-1} are given. The assignments of the different bands are in agreement with previous assignments of aromatic derivatives, observed isotopic effects, and INS results.^{27,28} Among these modes, the out-of-plane bendings γ_{CC} 16b and 16a according to Wilson's notation⁶⁸ at respectively ca. 520 and 420 cm^{-1} and γ_{CH} (11) at ca. 830 cm^{-1} are expected to be sensitive to the environment, particularly to the static intra- and intermolecular disorder. These bands are very broad and present several components. The origin of the splitting can be found in the presence of different aromatic cycles. It cannot be a site effect because the splitting is also present in the THF solution spectra (Figure 10a). The bands assigned to the vibrations of d type (δ_{cc}) are also broad except for the 748 cm^{-1} band in the EB Raman spectrum. The intensity of this band increases as the excitation wavelength increases. The band does not exist in the Raman spectra of the ES

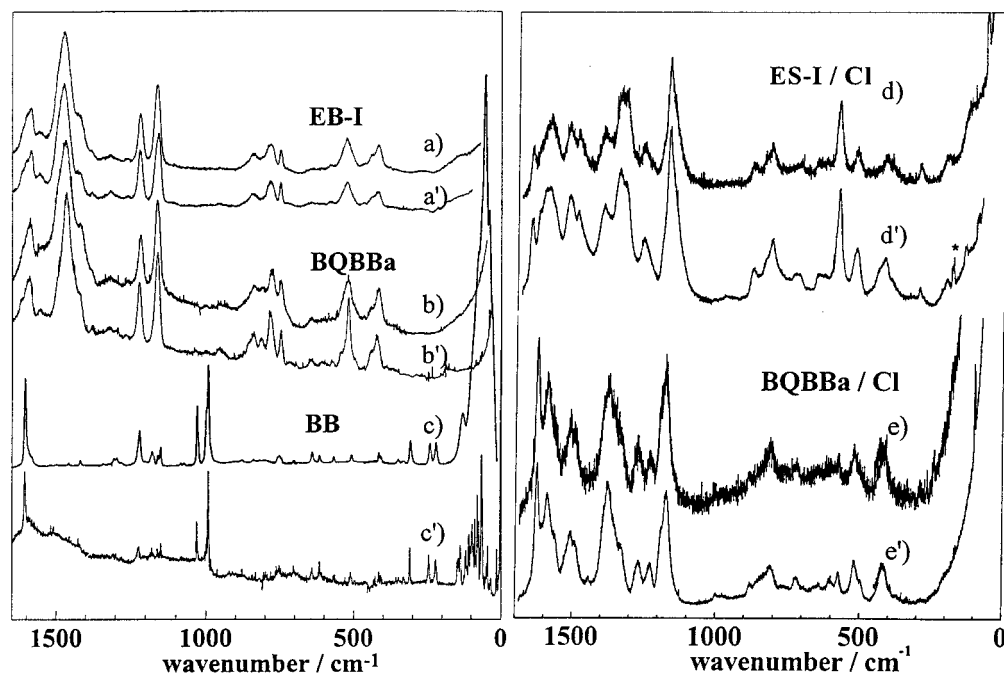


Figure 12. Comparison of room temperature (a, b, c, d, e) and ~50 K (a', b', c', d', e') Raman spectra ($\lambda_{\text{exc}} = 632 \text{ nm}$, $P = 5 \text{ mW}$) for EB-I (a, a') and ES-I (d, d'), BQBBa (b, b'), and its chloride salt (e, e') and BB (c, c').

form. No counterpart is observed in INS spectra^{27,28} which confirm that this mode does not involve proton motion. Thus, it can reasonably assume that it corresponds to the in-plane ring deformation of the semi-quinoid part of the exciton. Its narrowness indicates a well-defined geometry.

The spectral changes versus temperature make it possible to compare dynamic (temperature dependent) and static (temperature independent) disorders present in the PANI and its oligomers. BB, BQBBa, and EB-I Raman spectra ($\lambda_{\text{exc}} = 632.81 \text{ nm}$) recorded at room and helium temperature (~50 K) in the range 0–1700 cm^{-1} are given in Figure 12. According to the usual feature, the BB spectrum shows a considerable band narrowing passing from room (Figures 12c) to helium temperature (Figures 12c'), while the EB-I spectrum remains broad even at "helium" temperature (Figure 12a'), and intermediate behavior is observed for the BQBBa spectrum (Figure 12b,b'). Figure 13 displays the room and helium temperature full width at half-maximum (fwhm) of the bands observed between 850 and 400 cm^{-1} for BB, BQBBa, and EB-I polymer. The temperature effect on BB and BQBBa spectra is obvious. On the contrary, no change is observed in the EB-I spectrum. This is proof that there is a large static disorder in polymeric material and essentially dynamic disorder in oligomer. As far as the salts are concerned, the bandwidths remain nearly constant, even for the oligomer (Figure 12).

The Raman spectrum of a material composed of segregated crystalline and amorphous regions is expected to be the superposition of narrow (crystalline) and broad (disordered) components if the light penetrates both regions equally. Such behavior is not observed in the EB-I spectrum (except the 748 cm^{-1} band) or in the ES-I, II ones. This agrees with the concept of continuous, progressive intrachain orientational disorder proposed for the understanding of the X-ray powder patterns. The spectral broadening depends mainly on the type of motion. As expected, the out-of-plane deformations are very sensitive to the

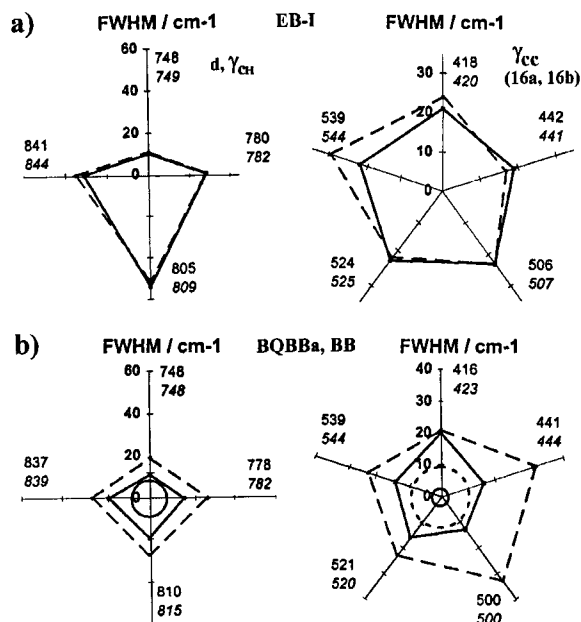


Figure 13. Raman ($\lambda_{\text{exc}} = 632.81 \text{ nm}$) full width at half-maximum (fwhm) of ring deformation modes (400–600 cm^{-1} region) and ring/CH deformation modes (700–850 cm^{-1}) at room temperature (dotted line) and at ~50 K (full line) for (a) EB-I, (b) BQBBa and BB (circles).

environment. In conclusion, from the vibrational point of view, the dynamic disorder observed in BQBBa and smaller ring associated moieties becomes static in polyaniline.

3.6. Assignment of the Low Wavenumber Excitations. According to our preliminary report on INS and IR reflectivity of ES-II HSO_4 powder,^{27,28} all emeraldine salts IR spectra exhibit a band at ca. 150 cm^{-1} , with some shoulders (Figure 11). Its strong IR intensity shows that dipolar species are involved in the motion, and the observation of the INS counterpart^{27,28} indicates that hydrogen motion is also involved. On the contrary, the IR spectra of neutral emeraldine base (EB-I, EB-II)

Table 3. IR Reflectivity, Raman, and INS Band Wavenumbers and Assignments in the Deformation and Lattice Mode Range for Salt Forms

IR ^a							Raman ^b										INS ^c ES-I	assignments
ES-I						ES-II	solutions		ES-I				ES-II					
HSO ₄	CSA	Cl(H)	Cl(D)	ρ^d	Cl(D,N ¹⁵)	Cl	CH ₃ SO ₃ H	H ₂ SO ₄	Cl(H)	Cl(D)	ρ^d	CSA	HSO ₄	Cl				
826 m	825 m	824 m	738 sh	1.11	738 sh	825 m	830 m						854 m	848 m	830 m	γ_{CH}		
807 m	805 m	805 m	719 m	1.11	719 m	803 m	805 m	809 m	809 m			811 m	816 m	809 m				
713 w	712 w	713 w				712 w	721 m	726 m	710 w			712 m	714 m	715 m	718 w	ring def (d)		
591 m									588 m			585 m	583 m	577 m				
520 m	521 m	517 m	446 m	1.16	445 m	515 m	517 m	510 m	516 m	443 m	1.16	517 m	515 m	518 m	522 s	γ_{CC} (16b)		
			394 w		390 w		443 w	445 w										
414 m	413 m	413 m	361 w	1.14	364 w	408 m	415 m	406 m	413 m	366 m	1.13	425 m	418 m	417 m	420 s	γ_{CC} (16a)		
															350 w			
									296 m	278 m	1.06	296 vw		295 vw	284 w			
	206 w	213 w	214 w	1	215 w		180 w	162 w	200 m	187 m	1.07	202 m			206 w	$C_{ar}NC_{ar}$ deformation and lattice modes		
125 s	103 s	158 s	147 s	1.07	139 s	135 s			120 m			119 m	147 m	146 m				

^a Reflection IR spectra converted into dielectric function by Kramers–Kronig transformation, room temperature. ^b 633 nm exciting wavelength, room temperature. ^c 20 K inelastic neutron scattering from refs 27 and 28. ^d Isotopic ratio. Along the rings are deuterated. ^e s = strong, m = medium, w = weak, vw = very weak, sh = shoulder.

forms show in the same range a very small component (Figure 11a,a'). Ghosh et al.⁶⁹ have recently proposed an assignment of this band to the stretching mode of an interchain N–H···N hydrogen bond. This assumption has been soon considered by Sauvajol et al.,⁷⁰ who observed the 150 cm⁻¹ band in the inelastic neutron spectrum of stretched polyaniline EB-II films. Comparison of spectra of specifically deuterated rings and ¹⁵N derivatives (Table 3) shows an isotopic shift, consistent with a motion involving both aromatic cycles and nitrogen atoms. Spectra of emeraldine salts with anions of approximately similar radius but of different mass (e.g., Cl, CSA) show a slight mass effect (Table 3). This confirms inelastic neutron scattering experiments which ruled out the hypothesis of a strong N–H···N bond, at least at 20 K.^{27,28} So, this band cannot be assigned to an interchain N–H···N motion and involves both anion and cycles motions.

In addition to the ca. 150 cm⁻¹ band, in EB-I or EB-II base IR spectra (Figure 11a,a'), we can also observe a band at 80 cm⁻¹, better defined in the EB-II spectrum, due to the higher crystallinity. The deconvolution of salt spectra also shows the presence of a band at ca. 80 cm⁻¹, which is not sensitive to D and ¹⁵N isotopic substitution. Ginder et al.⁷¹ have calculated for the leucoemeraldine (polyaniline reduced form) a Raman-active torsional mode in which adjacent phenyl rings oscillate out-of-phase. With the moment of inertia $I \sim 89$ amu Å² for phenyl ring rotations around the C–N axis, the expected wavenumber of this mode is ~ 90 cm⁻¹. Thus, we attribute the 80 cm⁻¹ band to a ring motion. Note that Sauvajol et al.⁷⁰ with incoherent inelastic-neutron-scattering data from stretch-aligned polyaniline base films have assigned two peaks at 80 and 56 cm⁻¹ to phenyl-ring librations around the single and double bonds, respectively. This point will be discussed further with the Rayleigh wing.

The low wavenumber band assigned to the C_{ring}–N–C_{ring} bending vibrations shifts down with temperature. Peak fitting of dielectric functions recorded for ES-I Cl pellet at 293 K and 10 K shows that the bands at 210 and 152 cm⁻¹ appear at 207 and 144 cm⁻¹ at 10 K (Figure 11d–d'). This unusual feature could indicate a structural rearrangement involving a change of electronic coupling of cycles.

3.7. Rayleigh Wing and Lattice Modes. When the considered compound have more than three cycles

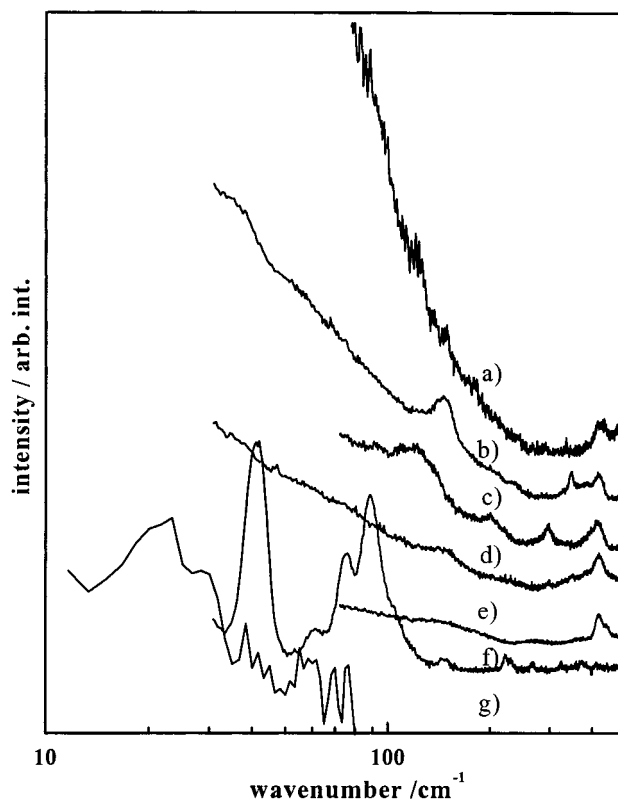


Figure 14. Room-temperature Raman spectra (632.81 nm, $P = 1$ mW) in the 10–450 cm⁻¹ range of BQBBa Cl (a), ES-II HSO₄ (b), ES-I Cl (c), ES-II Cl (d), EB-I (e), BBB (f) pellets and inelastic neutron scattering of a ES Cl film (g).

(benzenoid, quinoid, or semiquinoid), a drastic change appears in the low wavenumber Raman scattering. This phenomenon is particularly obvious when the Raman spectra are logarithmically plotted as a function of the wavenumber (Figure 14). The low-frequency scattering spectrum of BBB shows well-defined lattice modes, as is expected from a crystalline compound, while for the other compounds (BQBBa Cl, EB-I, ES-I Cl, ES-II Cl, ES-II HSO₄), the Rayleigh wing starts from 80 cm⁻¹. This is consistent with the corresponding X-ray powder patterns, which show well-defined Bragg's peaks for BBB and more or less broad features for the others. The wing slope is high for EB-I, ES-I Cl, ES-II Cl materials and is significantly greater for BQBBa Cl and ES-II

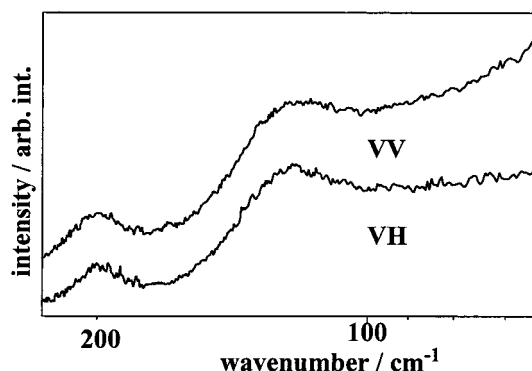


Figure 15. Raman polarized spectra (632.81 nm, $P = 1$ mW) of an ES-I HSO_4 pellet at room temperature.

HSO_4 . ES-I Cl, ES-II Cl, and ES-II HSO_4 materials have approximately the same degree of crystallinity ($X_c \sim 50\%$), but the ES-II HSO_4 diffractogram (Figure 8g) presents larger correlation lengths. Consequently, the dramatic climb of the Rayleigh wing is concerned by the short-range order concept. This lead us to study specifically the origin of this feature.

Inelastic light scattering from condensed matter is due to fluctuations of the dielectric susceptibility which, in turn, are related to the spectrum of dynamic excitations of the system. In crystals, momentum conservation during the scattering event only allows zone-center phonons to be Raman-active while acoustic modes are inactive. Structure disorder such as stacking fault induces the Brillouin zone folding; hence, some optical phonons become active. These restrictions are removed in amorphous solids, and all modes could be active. Basically, it is assumed that it is the local disorder of amorphous materials which gives electric and mechanic fluctuations. These fluctuations destroy the symmetry rules which explain that the acoustic modes give rise to Raman scattering. In strong glasses, this gives the so-called Boson peak.^{72–74} In liquids, the viscous damping of hydrodynamic modes leads to broadening of the Brillouin lines and the appearance of the quasi-elastic Rayleigh component. This implies that the quasielastic component and the Boson peak are intimately related.⁷⁵ As a consequence, their depolarization ratios (VV/VH) are generally similar. Consequently, the depolarized spectrum (VH) more closely reflects the density of states of the system than the polarized (elastic) line. For illustration, in Figure 15 is compared the VV and VH spectra of the ES-I/ HSO_4 salt. (Intensity has been corrected from the spectrometer response.) The Rayleigh wing appears to have a stronger VV character which rules out the assignment to a Boson peak feature or to a density-of-state contribution.

Translational or librational modes of entities (anions, chains) located in small potential well can be considered. The Raman spectra of ion exchangers and of superionic conductors show overdamped low wavenumber translational modes which can give rise to a strong Rayleigh wing if the polarizability of the considered species is large.⁷⁶ The polarizability of anions (of the Cl or HSO_4 type) is too low to give rise to such strong bands. On the other hand, due to their π electron cloud, aromatic cycles exhibit high polarizability. However, the Raman spectra of BB and BBB (Figures 12 and 14) show huge bands between 50 and 10 cm^{-1} . Solid aniline itself exhibits a similar feature.⁷⁷ We propose to assign the strong low-frequency wing to overdamped lattice modes,

because it roughly shifts according to the law of weights when we are considering the BB–BBB series, rather than to an isolated ring librational mode, which frequency is expected to remain constant or to increase when the length of the chain increases its stiffness. The high intensity of these bands indicates that the motion involves a strong deformation of the aromatic electronic shell associated with the ring motions. The broadening will result from the short-range disorder which modulates the “crystalline” field, the potential well of the modes involving the motion of aromatic units.

Preliminary inelastic neutron scattering experiments⁷⁸ performed on oriented ES film on the 3 axis spectrometer of the Leon Brillouin CEA-CNRS laboratory confirms that low-frequency modes occur below 100 cm^{-1} (Figure 14g) at 75, 70, 55, 38, 30, and 25 cm^{-1} . The lowest frequency mode shifts with unit-cell mass. This is consistent with an assignment to a translation motion of the four-cycle unit cell. Thus, the strong Rayleigh wing arises from the overlap of low-frequency modes with a true Rayleigh band arising from the dielectric heterogeneity of the materials (presence of metallic islands in a semiconducting medium).

Conclusion

The ring deformation and lattice libration modes region appears very useful for the understanding of the short-range structure of polyaniline. ES-I and ES-II allotropic forms are easily distinguished on the basis of their vibrational spectra. Although the bandwidth of polymer spectra does not depend on temperature in the 50–300 K explored temperature range, a strong reduction of the full width at half-height is measured for the BB and BQBBa, which confirms that part of the dynamic disorder of aromatic rings becomes static in polymers. This is consistent with the geometric models leading to a paracrystal sketch, i.e., a continuous deformation of the periodic chain configuration in place of an irregular pavement of amorphous and crystalline regions. Consequently, the identification of the conducting zones with “crystalline” regions is not pertinent. The chain curvature is fixed in the polymeric chains during the synthesis step of the pristine material and determines the structure or the disorder. The strong Rayleigh wing arises from the short-range disorder and from the presence of dielectric heterogeneities which broadens and makes difficult the observation of the librational and lattice modes involving the motion of aromatic cycles. These modes are resolved in inelastic neutron scattering spectra of oriented polyaniline (ES film). The spectroscopic unit appears to be limited to a two-cycle chemical unit. IR reflectivity shows unusual feature between 20 and 100 K, which can be related to an electronic/structural change at low temperature. The description in terms of nondirectionally bonded and “mechanically free” protons allows to understand the interactions between electronic–protonic delocalization and the conformation.

Acknowledgment. Dr. D. Michel and A. Régis are kindly acknowledged for fruitful discussions and F. Romain and J. P. Brun for their technical help. Dr. B. Hennon is acknowledged for his help in the recording of the low-frequency inelastic neutron scattering spectrum.

References and Notes

- (1) MacDiarmid, A. G.; Epstein, A. J. *Faraday Discuss. Chem. Soc.* **1989**, *88*, 317.

- (2) Furukawa, Y. *Synth. Met.* **1995**, *69*, 629–632.
- (3) Genies, E. M.; Lapkowski, M.; Tsintaris, C. *New J. Chem.* **1988**, *12*, 181–196.
- (4) Doriomedoff, M.; Hautière-Cristofini, F.; de Surville, R.; Josefowicz, M.; Yu, L. T.; Buwet, R. *J. Chim. Phys.* **1971**, *62*, 1055–1089.
- (5) Andrieu, X.; Josset, L.; Fauvarque, J. F. *J. Chim. Phys.* **1995**, *92*, 879–882.
- (6) Shimidzu, T. *Pure Appl. Chem.* **1995**, *67* (12), 2039–2045.
- (7) Cao, Y.; Treacy, G. M.; Smith, P.; Heeger, A. J. *Appl. Phys. Lett.* **1992**, *60* (22), 2711–2713.
- (8) Lavrencic-Stangar, U.; Orel, B.; Régis, A.; Colomban, Ph. *J. Sol. Gel Sci. Technol.* **1997**, *8*, 1965.
- (9) Matsunaga, T.; Daifuku, H.; Nakajima, T.; Kawagoe, T. In *Polymers for Advanced Technologies*; John Wiley & Sons Ltd: New York, 1990; Vol. 1, pp 33–39.
- (10) Roth, S. In *One-dimensional Metals*; VCH: Weinheim, 1995; pp 216–217.
- (11) Gregory, R. V.; Kimbrell, W. C.; Kuhn, H. H. *Synth. Met.* **1989**, *28*, C823.
- (12) Racicot, R.; Clark, R. L.; Liu, H. B.; Yang, S. C.; Alias, M. N.; Brown, R. *SPIE Proc.* **1995**, *2528*, 251.
- (13) Racicot, R.; Alias, M. N.; Brown, R.; Clark, R. L.; Liu, H. B.; Yang, S. C. *Proc. Mater. Res. Soc.* **1996**, *413*, 529–534.
- (14) Ahmad, N.; MacDiarmid, A. G. *Synth. Met.* **1996**, *78*, 103–110.
- (15) Wessling, B. *Adv. Mater.* **1994**, *6*, 226.
- (16) Neoh, K. G.; Kang, E. T.; Tan, K. L. *Polymer* **1993**, *34*, 1630.
- (17) Nechtschein, M.; Genoud, F.; Menardo, G.; Mizoguchi, K.; Travers, J. P.; Villeret, B. *Synth. Met.* **1989**, *29*, E211.
- (18) Jozefowicz, M. E.; Laversanne, R.; Javadi, H. H. S.; Epstein, A. J.; Pouget, J. P.; Tang, X.; MacDiarmid, A. G. *Phys. Rev. B* **1989**, *39*, 12958.
- (19) Pouget, J. P.; Jozefowicz, M. E.; Epstein, A. J.; Tang, X.; MacDiarmid, A. G. *Macromolecules* **1991**, *24*, 779–789.
- (20) Colomban, Ph.; Folch, S.; Gruger, A.; Régis, A.; Michel, D. *C. R. Acad. Sci. Paris* **1996**, *322*, IIB, 63–70.
- (21) Oh, E. J.; Min, Y.; Wiesinger, J. M.; Manohar, S. K.; Scherr, E. M.; Prest, P. J.; MacDiarmid, A. G.; Epstein, A. J. *Synth. Met.* **1993**, *55–57*, 977.
- (22) Laridjani, M.; Pouget, J. P.; Scherr, E. M.; MacDiarmid, A. G.; Jozefowicz, M. E.; Epstein, A. J. *Macromolecules* **1992**, *25*, 4106.
- (23) Epstein, A. J.; Ginder, J. M.; Zuo, F.; Bigelow, R. W.; Woo, H.-S.; Tanner, D. B.; Richter, A. F.; Huang, W.-S.; MacDiarmid, A. G. *Synth. Met.* **1987**, *18*, 303.
- (24) Ginder, J. M.; Richter, A. F.; MacDiarmid, A. G.; Epstein, A. J. *Solid State Commun.* **1987**, *63* (2), 97.
- (25) Epstein, A. J.; MacDiarmid, A. G. *Synth. Met.* **1995**, *69*, 179.
- (26) Holland, E. R.; Monkman, A. P. *Synth. Met.* **1995**, *74*, 75.
- (27) Baddour-Hadjean, R.; Fillaux, F.; Colomban, Ph.; Gruger, A.; Régis, A.; Parker, S. F.; Yu, L. T. *Synth. Met.* **1996**, *81*, 211–214.
- (28) Fillaux, F.; Leygue, N.; Baddour-Hadjean, R.; Parker, S.; Colomban, Ph.; Gruger, A.; Régis, A.; Yu, L. T. *Chem. Phys.* **1997**, *216*, 281.
- (29) Fillaux, F.; Ouboumour, H.; Tomkinson, J.; Yu, L. T. *Chem. Phys.* **1991**, *149*, 459.
- (30) Colomban, Ph.; Tomkinson, J. *Solid States Ionics* **1997**, *97*, 123.
- (31) Hinrichs, R.; Régis, A.; Gruger, A.; Colomban, Ph. *Synth. Met.* **1996**, *81*, 227–231.
- (32) Saprigin, A.; Kohlman, R. S.; Long, S. M.; Brenneman, K. R.; Epstein, A. J.; Angelopoulos, M.; Liao, Y.-H.; Zhang, W.; A.G. MacDiarmid, A. G. *Synth. Met.* **1997**, *84*, 767.
- (33) Malmonge, J. A.; Mattoso, L. H. C. *Synth. Met.* **1997**, *84*, 779.
- (34) Colomban, Ph.; Gruger, A.; Novak, A.; Régis, A. *J. Mol. Struct.* **1994**, *317*, 261–271.
- (35) Gruger, A.; Novak, A.; Régis, A.; Colomban, Ph. *J. Mol. Struct.* **1994**, *328*, 153–167.
- (36) Long, S. M.; Brenneman, K. R.; Saprigin, A.; Kohlman, R. S.; Epstein, A. J.; Angelopoulos, M.; Buchwalter, S. L.; Rossi, A.; Zheng, W.; MacDiarmid, A. G. *Synth. Met.* **1997**, *84*, 809.
- (37) Cao, Y.; Andreatta, A.; Heeger, A. J.; Smith, P. *Polymer* **1989**, *30*, 2305–2311.
- (38) Selvan, S. T.; Mani, A.; Athinearayanamsamy, K.; Phani, K. L. N.; Pitchumani, S. *Mater. Res. Bull.* **1995**, *30*, 699–705.
- (39) Honzl, J.; Tlustakova, M. *J. Polym. Sci.* **1968**, *22*, 451.
- (40) Zhang, W. J.; Feng, J.; MacDiarmid, A. G.; Epstein, A. J. *Synth. Met.* **1997**, *84*, 119–120.
- (41) Amano, K.; Ishikawa, H.; Kobayashi, A.; Satoh, M.; Hasegawa, E. *Synth. Met.* **1994**, *62*, 229–232.
- (42) Kulkarni, Vaman, G.; Mathew, W. *Synth. Met.* **1991**, *41–43*, 1009–1012.
- (43) Rodrigue, D.; Riga, J.; Verbist, J. J. *J. Chem. Phys.* **1992**, *89*, 1209–1214.
- (44) Abell, L.; Pomfret, S. J.; Adams, P. N.; Monkman, A. P. *Synth. Met.* **1997**, *84*, 127.
- (45) Colomban, Ph.; Badot, J. C. In *Proton Conductors*; Colomban, Ph., Ed.; Cambridge University Press: Cambridge, 1992; Chapter 25, p 389.
- (46) Epstein, A. J.; MacDiarmid, A. G. In Salaneck, W. R., Clark, D. T., Samvelsen, E. J., Eds. *Science and Applications of Conducting Polymers*; Proc. 6th Europhysics Industrial Workshop, Lofthus, May 1990; Adam Hilger: London, p 141.
- (47) Von Hosemann, R. *Acta Crystallogr.* **1951**, *4*, 520.
- (48) Guinier, A. In *Theorie et technique de la Radiocristallographie*; Dunod: Paris, 1956; p 617.
- (49) Colomban, Ph.; Efremova, A.; Gruger, A.; Novak, A. *Solid State Ionics* **1995**, *78*, 19–30.
- (50) Regho, M.; Cao, Y.; Moses, D.; Heeger, A. J. *Phys. Rev.* **1993**, *B47*, 1758.
- (51) Kohlman, R. S.; Epstein, A. J. In *Handbook of Conducting Polymers*; Marcel Dekker Inc.: New York, 1997; Chapter 3, pp 85–121.
- (52) Colomban, Ph.; Gruger, A.; Régis, A. *C. R. Acad. Sci. Paris* **1995**, *321*, Sér. IIB, 247–254.
- (53) Duke, C. B.; Conwell, E. M.; Paton, A. *Chem. Phys. Lett.* **1986**, *131*, 82.
- (54) Cao, Y.; Li, S.; Xue, Z.; Guo, D. *Synth. Met.* **1986**, *16*, 305.
- (55) Kim, Y. H.; Foster, C.; Chiang, J.; Heeger, A. J. *Synth. Met.* **1989**, *29*, E285.
- (56) Stafström, S.; Sjögren, B.; Brédas, J. L. *Synth. Met.* **1989**, *29*, E219.
- (57) Jozefowicz, M. E.; Epstein, A. J.; Pouget, J. P.; Masters, J. G.; Ray, J. G.; MacDiarmid, A. G. *Macromolecules* **1991**, *24*, 5863.
- (58) Pouget, J. P.; Oblakowski, Z.; Nogami, Y.; Albouy, P. A.; Laridjani, M.; Oh, E. J.; Min, Y.; MacDiarmid, A. G.; Tsukamoto, J.; Ishiguro, T.; Epstein, A. J. *Synth. Met.* **1994**, *65*, 131–140.
- (59) Pouget, J. P.; Hsu, C.-H.; MacDiarmid, A. G.; Epstein, A. J. *Synth. Met.* **1995**, *69*, 119–120.
- (60) Djurado, D.; Nicolau, Y. F.; Dalsegg, I.; Samuelsen, E. J. *Synth. Met.* **1997**, *84*, 121–122.
- (61) Minto, C. D. G.; Vaughan, A. S. *Polymer* **1997**, *38*, 11, 2683–2688.
- (62) Furakawa, Y.; Hana, T.; Hyodo, Y.; Harada, I. *Synth. Met.* **1986**, *16*, 189.
- (63) Furakawa, Y.; Ueda, F.; Hyodo, Y.; Harada, I.; Nakajima, T.; Kawagoe, T. *Macromolecules* **1988**, *21*, 1297.
- (64) Harada, I.; Furakawa, Y.; Ueda, F. *Synth. Met.* **1989**, *29*, E303–E312.
- (65) Louarn, G.; Lapkowski, M.; Quillard, S.; Pron, A.; Buisson, J. P.; Lefrant, S. *J. Phys. Chem.* **1996**, *100*, 6998.
- (66) Perrier-Datin, A.; Lebas, J. M. *J. Chim. Phys.* **1972**, *4*, 591.
- (67) Choi, C. H.; Kertesz, M. *Macromolecules* **1997**, *30*, 620–630.
- (68) Varsanyi, G. In *Assignments for Vibrational Spectra of Benzene Derivatives*; Adam Hilger: London, 1987; Vol. 1.
- (69) Ghosh, S.; Bowmaker, G. A.; Cooney, R. P. *J. Mater. Chem.* **1997**, *7*, 597.
- (70) Sauvajol, J. C.; Djurado, D.; Dianoux, A. J.; Fischer, J. E.; Scherr, E. M.; MacDiarmid, A. G. *Phys. Rev. B* **1993**, *47* (9), 4959.
- (71) Ginder, J. M.; Epstein, A. J. *Phys. Rev.* **1990**, *B41*, 10674.
- (72) Jackle, J. In *Amorphous Solids: Low-Temperature Properties*; Philipps, W. A., Ed.; Springer: Berlin, 1981; p 135.
- (73) Malinovsky, V. K.; Sokolov, A. P. *Solid State Commun.* **1986**, *57*, 757.
- (74) Sokolov, A. P.; Kisliuk, A.; Quitmann, D.; Duval, E. *Phys. Rev.* **1993**, *B48*, 7692.
- (75) Brodin, A.; Torrell, L. M. *J. Raman Spectrosc.* **1996**, *27*, 723–730.
- (76) Colomban, Ph.; Lucazeau, G. *J. Chem. Phys.* **1980**, *72*, 1213.
- (77) Tripathi, G. N. R. *J. Chem. Phys.* **1990**, *73* (11), 5521.
- (78) Colomban, Ph.; Hennion, B., unpublished results.